



ELSEVIER

Contents lists available at ScienceDirect

Journal of Petroleum Science and Engineering

journal homepage: www.elsevier.com/locate/petrol

Breakdown pressures due to infiltration and exclusion in finite length boreholes

Quan Gan ^{a,*}, Derek Elsworth ^a, J.S. Alpern ^b, Chris Marone ^b, Peter Connolly ^c^a Department of Energy and Mineral Engineering, EMS Energy Institute and G3 Center, The Pennsylvania State University, University Park, PA 16802, USA^b Department of Geosciences, G3 center and EMS Energy Institute, The Pennsylvania State University, University Park, PA 16802, USA^c Chevron Energy Technology Company, Houston, TX 77002, USA

ARTICLE INFO

Article history:

Received 26 May 2014

Accepted 9 January 2015

Available online 16 January 2015

Keywords:

fracture breakdown pressure

supercritical fluid

subcritical fluid

Biot coefficient

finite borehole length

infiltration

extraction

ABSTRACT

The theory of effective stress suggests that the breakdown pressure of a borehole should be a function of ambient stress and strength of the rock, alone. However, experiments on finite-length boreholes indicate that the breakdown pressure is a strong function of fracturing fluid composition and state as well. The reasons for this behavior are explored, including the roles of different fluid types and state in controlling the breakdown process. The interfacial tension of the fracturing fluid is shown to control whether fluid invades pore space at the borehole wall and this in turn changes the local stress regime, hence breakdown pressure. Interfacial tension is modulated by fluid state, as sub- or super-critical, and thus gas type and state influence the breakdown pressure. Expressions are developed for the breakdown pressure in circular section boreholes of both infinite and finite length and applied to rationalize otherwise enigmatic experimental observations. Importantly, the analysis accommodates the influence of fluid infiltration or exclusion into the borehole wall. For the development of a radial hydraulic fracture (longitudinal failure), the solutions show a higher breakdown pressure for impermeable relative to a permeable borehole. A similar difference in breakdown pressure exists for failure on a transverse fracture that is perpendicular to the borehole axis, in this case modulated by a parameter η , which is a function of Poisson ratio and the Biot coefficient. These solutions are used to rationalize observations for mixed-mode fractures that develop in laboratory experiments containing finite-length boreholes. Predictions agree with the breakdown pressure records recovered for experiments for pressurization by CO₂ and Ar – higher interfacial tension for subcritical fluids requires higher critical pressures to invade into the matrix, while supercritical fluid with negligible interfacial tension has less resistance to infiltrate into the matrix and to prompt failure. This new discovery defines mechanisms of failure that although incompletely understood, provisionally link lower breakdown stresses with mechanisms that promote fracture complexity with the potential for improved hydrocarbon recovery.

© 2015 Elsevier B.V. All rights reserved.

1. Introduction

The breakdown pressure is the critical pressure where failure occurs during borehole pressurization. Numerous attempts have been made to forecast the magnitude of breakdown pressure by analytical, semi-analytical and numerical approaches (Kutter, 1970; Newman, 1971; Tweed and Rooke, 1973).

Initial attempts focused on an analytical formula to predict the breakdown pressure in impermeable rocks (Hubbert and Willis, 1957). Subsequent analyses extended this formula for fluid pressurization in permeable rocks (Haimson and Fairhurst, 1967). In

this solution, thermoelastic stressing was used as an analog to represent fluid pressurization (Timoshenko and Goodier, 1951). The results from these two approaches and for these two conditions – impermeable versus permeable borehole walls – show two different bounding values: the breakdown pressure in permeable rock is always lower than that in impermeable rock.

This approach provides a pathway to explore pressurization rate effect on the breakdown process. Experimental approaches have shown that at higher pressurization rates, the breakdown pressure is also elevated (Zoback et al., 1977; Solberg et al., 1980; Zeng and Roegiers, 2002; Wu et al., 2008). This observation may be explained as the influence of a pressure diffusion mechanism (Detournay and Cheng, 1992; Garagash and Detournay, 1996), that requires a critical diffusive pressure to envelop a critical flaw length in the borehole wall.

* Corresponding author. Tel.: +1 814 753 2258.

E-mail address: gxq5004@psu.edu (Q. Gan).

Nomenclature

α	Biot coefficient, dimensionless
ν	Poisson ratio, dimensionless
p_w	fluid pressure, MPa
E	Young's modulus, MPa
σ_T	rock tensile strength, MPa
$\sigma_{\theta\theta}$	tangential stress around wellbore, MPa
σ_{rr}	radial stress, MPa
σ_{zz}	longitudinal stress, MPa
k	permeability, m^2

μ	fluid viscosity, Pa s
ρ_f	fluid density, kg/m^3
K_S	grain bulk modulus, MPa
K	solid bulk modulus, MPa
K_f	fluid bulk modulus, MPa
r	wellbore radius, m
P_c	critical invasion pressure, MPa
n	porosity, dimensionless
P_b	breakdown pressure, MPa
u	displacement from solid deformation, m

All these approaches rely on Terzaghi's theory of effective stress (Biot, 1941), which predicts that failure will occur when the effective stress is equal to the tensile strength. Furthermore, this suggests that breakdown pressures should be invariant of fluid type (composition) or state (gas or liquid) since failure is mediated by effective stress, alone. However recent results (Alpern et al., 2012; Gan et al., 2013) suggest that fluid composition and/or state may influence breakdown pressure in an important manner. The flowchart in Fig. 1 shows the methodology and workflow involved in this work. The blue dashed rectangle identifies the state of the fluid and its influence on the breakdown pressure. In this work, we develop an approach to explain the role of fluid composition or state on breakdown pressure based on prior observations of permeable versus impermeable borehole walls. In this approach, the physical characteristics of the borehole remain the same for all fluid compositions, but the feasibility of the fluid either invading the borehole wall or being excluded from it changes with fluid state (subcritical or supercritical). An approach is developed based on Biot effective stress, to define breakdown pressure for supercritical/subcritical gas fracturing. The critical entry-pore pressure is governed by fluid interfacial tension (Berry et al., 1971; Escobedo and Mansoori, 1996; Bennion, 2006), and the subcritical fluid breakdown pressure is shown to scale with the critical fluid

invasion pressure. Breakdown pressures scaled in this manner agree with experimental observations.

2. Experimental observations

Fracturing experiments are reported on homogeneous cubes of polymethyl methacrylate (PMMA; Alpern et al., 2012). Fig. 2a depicts the configuration of specimens used in the experiments. The pressurized fracturing fluid is injected through a drilled channel, which is analogous to the borehole. The induced hydraulic fractures are embedded in cubes 101 mm (4 in.) and 121 mm (5 in.) on side. The borehole diameter is 3.66 mm, and the cubes are stressed under biaxial conditions σ_2 in the horizontal direction and σ_1 in the vertical direction. During the experiment, the stress state is $\sigma_2 = \sigma_1$, and $\sigma_3 = 0$ in the borehole-parallel direction. Fig. 2b shows the biaxial testing apparatus used in the experiment. Pore pressure is elevated with fluid injected under constant rate. Fracture occurs when the local borehole stresses exceeded the tensile strength of the PMMA, which is ~ 70 MPa. Fig. 2c and d shows the resulting fractures, both in the longitudinal mode and in transverse mode, respectively.

Six different fracturing fluids are injected in separate experiments and the borehole is pressurized to failure. The fluids used are helium (He), nitrogen (N_2), carbon dioxide (CO_2), argon (Ar), sulfur hexafluoride (SF_6), and water (H_2O). Fig. 3 illustrates the states of injected fluids based on the experimental data. In the experiments, nitrogen, helium and argon are supercritical at fracture breakdown, while sulfur hexafluoride, CO_2 and water are subcritical. The CO_2 experiments return the largest breakdown pressure of 70 MPa, while helium, nitrogen and argon fail at less than 33 MPa (Fig. 4). The tensile strength of PMMA is ~ 70 MPa.

The following observations are apparent from the experimental results:

1. The maximum breakdown pressure is obtained for CO_2 and is approximately equal to the tensile strength of the PMMA (~ 70 MPa).
2. The breakdown pressure for helium and nitrogen is approximately half of this tensile strength.

From these observations, we hypothesize that (1) the factor-of-two differential in the breakdown stresses results from infiltration versus exclusion of fluids from the borehole wall and (2) the different behaviors of infiltration versus exclusion result from the state of the fluid, super-critical versus sub-critical.

This hypothesis is explored by first identifying the difference in breakdown pressure for infiltrating versus non-infiltrating fluids and is then related to the propensity for infiltration *via* quantification of entry pressures in the borehole wall.

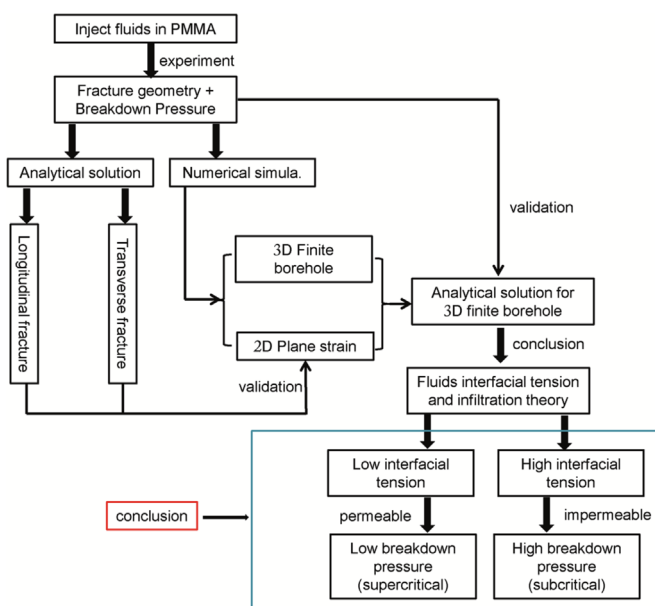


Fig. 1. Workflow initiating from the injection of fluids in PMMA. The final conclusions are highlighted in the blue rectangle. (For interpretation of the references to colour in this figure legend, the reader is referred to the web version of this article.)

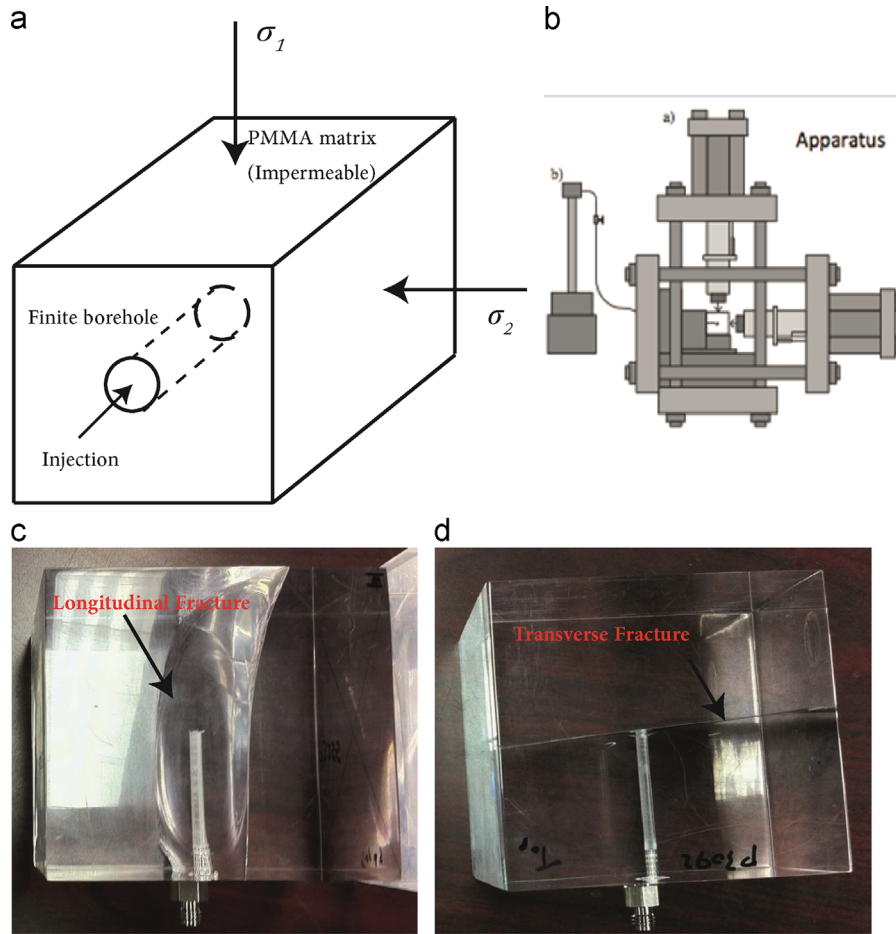


Fig. 2. (a) Schematic of PMMA specimen used in the experiment. The drilled borehole is located in the center of sample and terminates in the center of the cube. (b) Biaxial loading frame. Beryllium–copper load cells measure the applied force. PMMA cube is centered between the rams and attached to a pore pressure line with access through the front face of the cube. (c) Resulting longitudinal fracture in the PMMA sample parallel to the borehole direction. (d) Induced transverse fracture perpendicular to the drilled borehole in the PMMA sample.

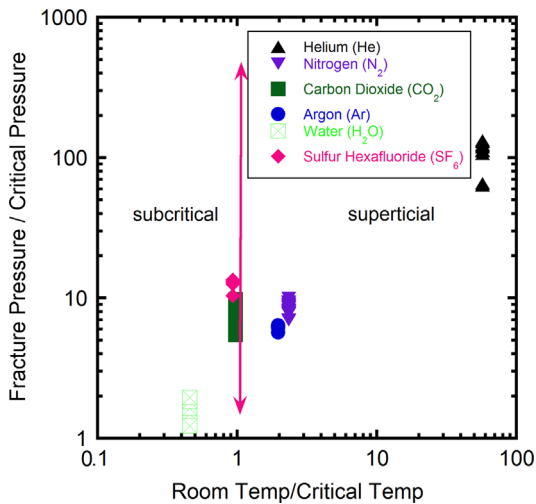


Fig. 3. Injected fracturing fluid state and properties under experiment condition. The fluid states are divided into subcritical state (left) and supercritical (right).

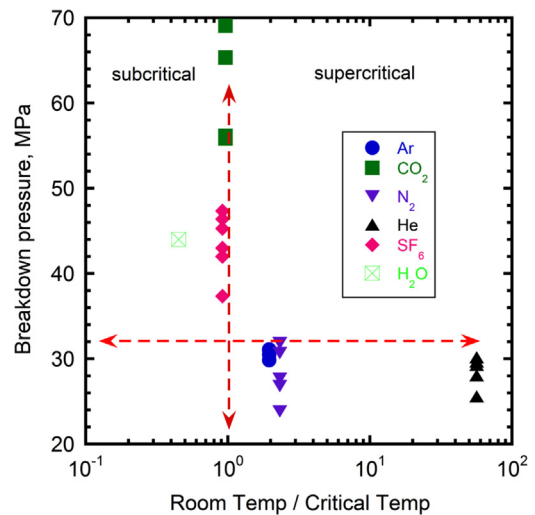


Fig. 4. Experiment results of fracture breakdown pressure under various injected fracturing fluids under the same experiment conditions (Alpern et al., 2012).

3. Analytical solutions

Consider a finite radius r_w borehole in an elastic domain (external radius r_e) under internal fluid pressure p_w , with the

domain confined under applied stresses σ_{11} and σ_{22} . Breakdown pressure may be defined for fracture both longitudinal to the borehole and transverse to it and for conditions where fluid infiltration is either excluded or allowed, as follows.

3.1. Fracture along borehole (longitudinal fracture)

For the longitudinal hydraulic fracture, breakdown occurs when the effective tangential stress is equal to the tensile strength. When the matrix is impermeable, there is no poroelastic effect and the solution is the Hubbert–Willis (H–W) (Hubbert and Willis, 1957) solution:

$$p_w = -3\sigma_{22} + \sigma_{11} + \sigma_T \quad (1)$$

where σ_{11} is the minimum principal stress, σ_{22} is the maximum principal stress, σ_T is the rock tensile strength, and p_w is required breakdown fluid pressure.

When the porous medium is permeable, the Biot coefficient α reflects the poroelastic effect. It shows the strongest poroelastic effect when $\alpha = 1$. The tangential total stress $S_{\theta\theta}$ is defined relative to the effective tangential stress $\sigma_{\theta\theta}$ and Biot coefficient α , as

$$S_{\theta\theta} = \sigma_{\theta\theta} - \alpha p_w. \quad (2)$$

The total stresses at the wellbore boundary are obtained by superposition of the stress fields from the Haimson–Fairhurst (H–F) solution (Haimson and Fairhurst, 1967) due to the total stresses σ_{11} and σ_{22} , fluid pressure p_w , and Poisson ratio ν as

$$S_{\theta\theta} = 3\sigma_{22} - \sigma_{11} - p_0 + p_w - \alpha p_w \frac{1-2\nu}{1-\nu}. \quad (3)$$

The effective tangential stress at the wellbore r_w is

$$\sigma_T = \sigma_{\theta\theta} = 3\sigma_{22} - \sigma_{11} - p_0 + p_w + \frac{\nu}{1-\nu} \alpha p_w. \quad (4)$$

Correspondingly, the breakdown pressure is

$$p_w = \frac{-3\sigma_{22} + \sigma_{11} + p_0 + \sigma_T}{1+\eta}. \quad (5)$$

where $\eta = \frac{\nu}{1-\nu} \alpha$.

This gives the appropriate breakdown pressures for cases where fluid is either excluded from the borehole wall (impermeable, Eq. (1), H–W) or allowed entry into the wall (permeable, Eq. (5), H–F).

3.2. Fracture across borehole (transverse fracture)

Where the fracture is transverse to the borehole then breakdown occurs when the longitudinal stress exceeds the tensile strength. The longitudinal stress σ_{zz} may be determined from the radial and tangential stresses. For the impermeable case, pressurization of the borehole wall results in equal increments and decrements of the radial and tangential stresses, respectively. This results in no net change in longitudinal stress.

However, for the condition of fluid infiltration, the longitudinal stress change is finite. The radial stress is defined as

$$\sigma_{rr} = -(1-\alpha)p_w. \quad (6)$$

The stress–strain relationship is defined from Hooke's law as

$$\varepsilon_{zz} = \frac{1}{E} [\sigma_{zz} - \nu(\sigma_{rr} + \sigma_{\theta\theta})]. \quad (7)$$

Since the longitudinal strain ε_{zz} is zero, the longitudinal stress is

$$\sigma_T = \sigma_{zz} = \nu(\sigma_{rr} + \sigma_{\theta\theta}) = \nu \left[(3\sigma_{22} - \sigma_{11} - p_0) + p_w + \frac{\nu}{1-\nu} \alpha p_w - (1-\alpha)p_w \right]$$

which may be transformed to give

$$\sigma_{zz} = \nu(3\sigma_{22} - \sigma_{11} - p_0) + \frac{\nu}{1-\nu} \alpha p_w. \quad (8)$$

Therefore, the breakdown pressure in terms of longitudinal stress is equal to

$$p_w = \frac{-\nu(3\sigma_{22} - \sigma_{11} + p_0) + \sigma_T}{\eta}. \quad (9)$$

Comparing Eqs. (5) and (9) illustrates that the breakdown pressure p_w for a longitudinal fracture is smaller than that for the transverse fracture. Therefore, fracture will always occur in the longitudinal direction before it can occur in the transverse direction, since $(1/(1+\eta))(Longitudinal) < (1/\eta)(transverse)$. This is the case for a borehole of infinite length but not necessarily for the finite-length boreholes examined in the experiments of this work.

4. Numerical model

The above expressions define the breakdown pressures for boreholes in infinite media. However the laboratory experiments are for blind and finite boreholes in cubic specimens. Therefore a finite element model is used to simulate the coupled process of fluid–solid interaction in geometries similar to the experiments. First, 2-D problems are explored to validate the model and then 3-D geometries are used to replicate the experiments and then to interpret the experimental observations.

4.1. 2-D model (plane strain)

A 2-D poro-mechanical model is used to represent the behavior with a central borehole within a square contour. The governing equations and boundary conditions are as follows.

4.1.1. Governing equation

Two governing equations represent separately the fluid flow and solid deformation processes. A Darcy flow model is applied to represent fluid flow with the Biot–Willis coefficient defined as

$$\alpha = 1 - \frac{K}{K_S}. \quad (10)$$

where K_S and K are identified as the grain and solid bulk modulus, respectively.

The flow equation is

$$S_\alpha \frac{\partial p}{\partial t} + \nabla \cdot \left[-\frac{k}{\mu} \nabla p \right] = -Q_s. \quad (11)$$

where p is the fluid pressure (Pa), k is the permeability (m^2), μ is the fluid viscosity (Pa s) and S_α is the skeletal component of specific storage (Leake and Hsieh, 1997) ($S_\alpha = (1/\rho_f g) (((\alpha-n)/K_S) + (n/K_f))$ where n is the porosity, ρ_f is the fluid density, g is the gravitational acceleration, K_S is the solid bulk modulus, and K_f is the fluid bulk modulus), and Q_s defines the time rate of change of volumetric strain from the equation for solid displacements,

$$Q_s = \alpha(d(u_x, t) + d(v_y, t)). \quad (12)$$

where the volume fraction of liquid changes with deformations u_x and v_y .

The solid deformation equation is

$$\frac{E}{2(1+\nu)} \nabla^2 u + \frac{E}{2(1+\nu)(1-2\nu)} \nabla \cdot (\nabla u) = \alpha \nabla p.$$

where E is Young's modulus, u is the displacement vector composed of orthogonal displacements u and v (m). The right hand side term $\alpha \nabla p$ represents the fluid-to-structure coupling term in terms of the gradient of pressure, ∇p . Recalling the previous analytical solutions for the required breakdown pressure, the breakdown pressure for the longitudinal fracture during injection is $p_w = ((-3\sigma_{22} + \sigma_{11} + p_0 + \sigma_T)/1+\eta)$, and the breakdown pressure for the transverse fracture is $p_w = ((-\nu(3\sigma_{22} - \sigma_{11} + p_0) + \sigma_T)/\eta)$.

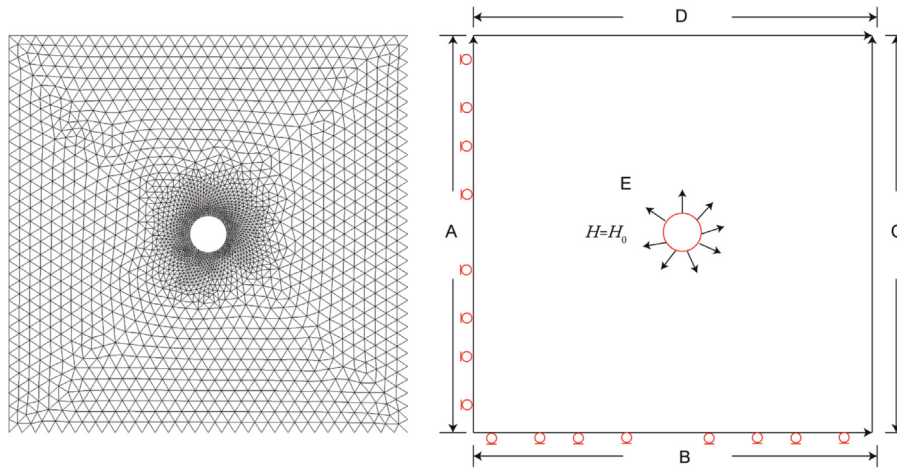


Fig. 5. 2-D Model geometry (left) created in simulations, and applied hydraulic and displacement boundary conditions and initial conditions (right).

Table 1
Hydraulic boundary and stress/displacement boundary applied in the COMSOL simulations.

Boundary	Stress boundary	Hydraulic boundary
A, B	$u_n = 0$	$n \cdot K \nabla H = 0$
C, D	Free	$n \cdot K \nabla H = 0$
E	Free	$H = H_0$

The final combined constitutive equations are obtained as below:

$$S_\alpha \frac{\partial p_w}{\partial t} + \nabla \cdot \left[-\frac{k}{\mu} \nabla p_w \right] = - [\alpha(d(u_x, t) + d(v_y, t))] \\ \frac{E}{2(1+\nu)} \nabla^2 u + \frac{E}{2(1+\nu)(1-2\nu)} \nabla \cdot (\nabla u) = \alpha \nabla p_w.$$

4.1.2. Boundary conditions

The 2-D plane strain model geometry comprises a slice-cut across a section (see Fig. 5). The left and basal boundaries A and B are set as roller condition with zero normal displacement (see Table 1). The interior circular boundary represents the borehole where fluid pressure p_w is applied uniformly around the contour. Table 2 shows the model input data. There is no confining stress applied to the outer boundary.

4.2. 2-D fracture breakdown pressure results

The 2-D simulation results are used to validate the model for the two forms of fractures – longitudinal versus transverse – evaluated previously. The likelihood of either failure model is controlled by either the tangential effective stress (longitudinal failure) or the longitudinal effective stress (transverse failure).

4.2.1. Validation for 2-D longitudinal fracture

Failure occurs when the tangential effective stresses reach the tensile strength at a critical location. The blue curve in Fig. 6 reflects the tangential effective stress calculated from the analytical solution (Eq. (4)). The analytical results give satisfactory agreement with the simulation results as shown by the red points. The curve shows that for a stronger poroelastic effect (increasing α), the tangential effective stress increases under the same fluid pressure.

Fig. 7 shows the effect of Poisson ratio on breakdown pressure, where the Poisson ratio ranges from 0.1 to 0.5. For constant Biot coefficient, a lower Poisson ratio will elevate the required breakdown

Table 2
PMMA properties used in the simulation.

Parameters	Value
Tensile strength, MPa	70
Fluid pressure, MPa	10
Poisson ratio	0.36
Young's modulus, Pa	3.0e9
Biot coefficient	0–1
Solid compressibility, 1/Pa	8e–11

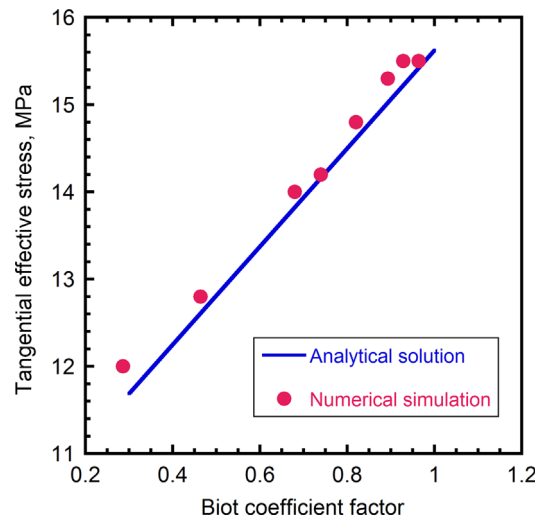


Fig. 6. Validation of 2-D tangential effective stress around borehole with various Biot coefficient factors (0.3–1). (For interpretation of the references to colour in this figure, the reader is referred to the web version of this article.)

pressure. The H–W equation for the impermeable case provides an upper bound for the stress scaling parameter of $1/(1+\eta)$ as unity. For a Poisson ratio equivalent to that of PMMA ($\nu = 0.36$), the simulation results define a breakdown pressure for the strongest poroelastic condition ($\alpha = 1$) as 0.65 times that for impermeable case.

4.2.2. Validation for 2-D transverse fracture

Fig. 8 shows the prediction of longitudinal effective stress under the constant fluid pressure of 10 MPa, and where the Biot coefficient varies from 0.2 to 1 for PMMA. The longitudinal stress from the simulation mimics the predictions from the analytical Eq. (8). This stress also grows with an increasing Biot coefficient.

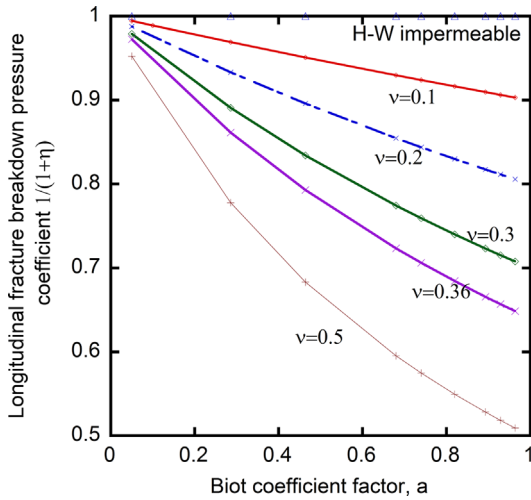


Fig. 7. Evolution of longitudinal fracture breakdown pressure coefficient with different Biot coefficients under various Poisson ratio (0–0.5) in permeable rocks.

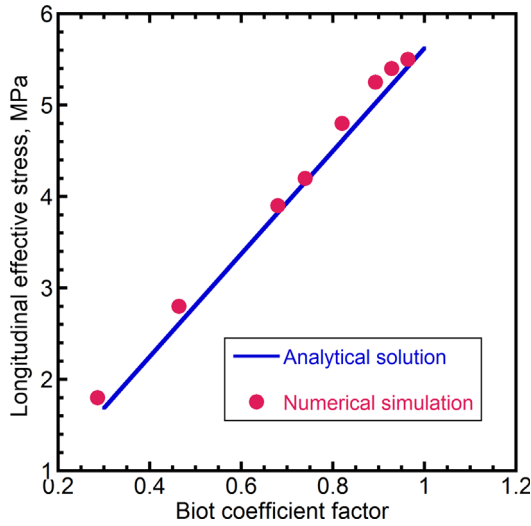


Fig. 8. Validation of 2-D longitudinal stress under different Biot coefficient factors (0.2–1).

The maximum longitudinal stress is lower than 6 MPa, which is half of the applied fluid pressure. The longitudinal stress is always lower than the tangential stress.

The proportionality of the longitudinal effective stress to the Biot coefficient for a transverse fracture is shown in Fig. 9 (see Fig. 7). This proportionality coefficient corresponds to the denominator in Eq. (9) as $1/\eta$. The magnitudes of this coefficient are unbounded as the Biot coefficient approaches zero, signifying zero poroelastic effect and an infinitely large pressure required for failure. Although longitudinal fracturing is the preferred failure mode for infinite boreholes, for finite boreholes transverse fracturing may be a significant mode.

4.3. Breakdown pressure for finite 3-D geometries

The failure conditions for a finite length borehole are now explored. The stress accumulation at the end of the borehole will be a combination of the modes represented in the longitudinal and transverse failure modes. The experimental configuration is for a finite-length end-capped borehole that terminates in the center of the block. We represent this geometry (see Fig. 10) with the plane with red set as roller boundaries (zero normal displacement condition).

For the finite borehole condition, the induced stresses may be shown to be a combination of the applied confining stress and

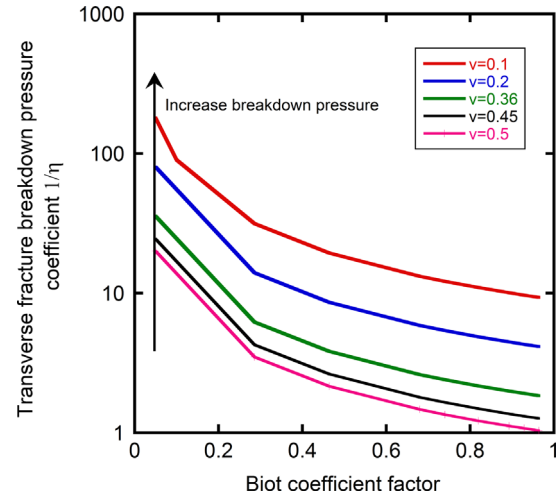


Fig. 9. Evolution of 2-D transverse fracture breakdown pressure coefficient under different Biot coefficient factors with Poisson's ratio ranging from 0.1 to 0.5 (longitudinal stress).

fluid pressure. The exact functional dependence may be obtained by the superposition of the confining stress field and the influence of fluid pressure in a simplified model.

Assuming the wellbore radius is equal to a , the radial and hoop stresses for a unidirectional confining stress σ_{11} are derived as below in polar coordinates (Jaeger and Cook, 1979):

$$\begin{aligned} \sigma_{rr} + \sigma_{\theta\theta} &= \sigma_{11} R_e \left\{ 1 - Ar^{-2} e^{-2i\theta} \right\} = \sigma_{11} (1 - Ar^{-2} \cos 2\theta) \\ \sigma_{\theta\theta} - \sigma_{rr} + 2i\sigma_{r\theta} &= \sigma_{11} \left[Br^{-2} - e^{2i\theta} + (Ar^{-2} + 3Cr^{-4})e^{2i\theta} \right] \end{aligned}$$

Then the top equation gives

$$\begin{aligned} \sigma_{\theta\theta} - \sigma_{rr} &= \sigma_{11} [Br^{-2} - (1 - Ar^{-2} - 3Cr^{-4}) \cos 2\theta] \\ \sigma_{r\theta} &= -\frac{1}{2}\sigma_{11} [(1 + Ar^{-2} + 3Cr^{-4}) \sin 2\theta] \end{aligned}$$

Since the borehole boundary at $r=a$ is traction-free, the stress σ_{rr} and $\sigma_{r\theta}$ must vanish at $r=a$; therefore, we can solve the equation to get the coefficients A, B, C to obtain the final expressions for the σ_{rr} and $\sigma_{\theta\theta}$.

$$\begin{aligned} \sigma_{rr} &= \frac{\sigma_{11}}{2} \left(1 - \frac{a^2}{r^2} \right) + \frac{\sigma_{11}}{2} \cos 2\theta \left(1 - \frac{a^2}{r^2} \right) \left(1 - 3\frac{a^2}{r^2} \right) \\ \sigma_{\theta\theta} &= \frac{\sigma_{11}}{2} \left(1 + \frac{a^2}{r^2} \right) - \frac{\sigma_{11}}{2} \cos 2\theta \left(1 + 3\frac{a^2}{r^2} \right) \end{aligned}$$

At the borehole wall $r=a$, the maximum and minimum stresses are at azimuths of $\theta=0^\circ$ and $\theta=90^\circ$, where tangential stresses around the borehole are $3\sigma_{11}$ and $-\sigma_{11}$, respectively. If a uniform confining stress is applied by adding a second confining stress ($\sigma_{11} - \sigma_{22}$), then the longitudinal and hoop stresses are

$$\begin{aligned} \sigma_z &= \nu(2\sigma_{11} + 0) \\ \sigma_\theta &= 2\sigma_{11} \end{aligned}$$

If the borehole is now pressurized by fluid, then the additional stresses are

$$\begin{aligned} \sigma_z &= \nu(p_w + (-p_w)) \\ \sigma_\theta &= -p_w \end{aligned}$$

Adding these two modes of solid stress and fluid pressure give the resulting longitudinal effective stress,

$$\sigma_z = 2\nu\sigma_{11} + p_w \cdot 0.$$

where the borehole end is capped (see Fig. 11), the longitudinal stress induced by internal fluid pressure will be augmented due to the effect of fluid pressures acting on the ends of the borehole. This

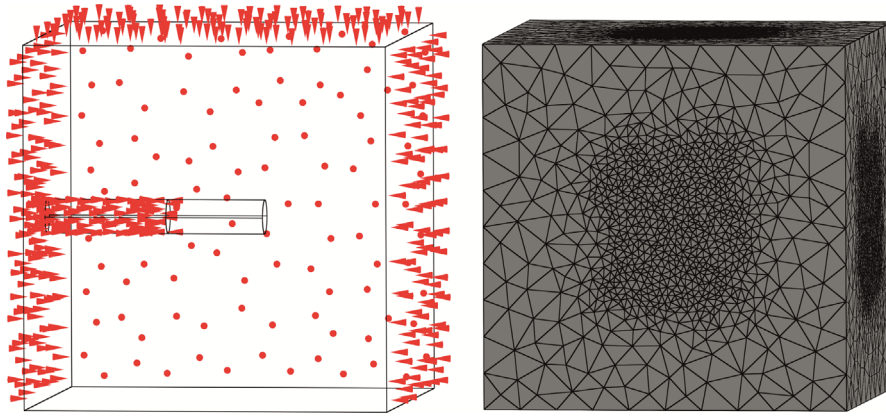


Fig. 10. 3-D model geometry with boundary condition (left), and mesh with finite borehole length condition (right). (For interpretation of the references to colour in this figure, the reader is referred to the web version of this article.)

equation for longitudinal stress is extended for the general case of a finite borehole by introducing the stress concentration factors B and C to calculate the maximum longitudinal stress in mixed plane strain–plane stress conditions for the actual geometry as

$$\sigma_z \text{ max} = -2\nu B\sigma_c + Cp_w \tag{13}$$

where B and C are coefficients recovered from the numerical modeling. The longitudinal effective stress is calculated at the end of borehole where fluid pressure is applied to obtain the longitudinal stress concentration factor (see Fig. 11). If confining stress is applied alone (without internal fluid pressure), then the geometric scaling coefficient for our particular geometry and for the maximum tensile tangential stress is $B=1.32$.

Fig. 11 shows the spatial distribution of the ratio σ_z/p_w in the domain. The maximum value represents the coefficient C in Eq. (13). Based on the above results: $C_{\text{permeable}} = 2.756$ and $C_{\text{impermeable}} = 1.328$. Assuming the tensile strength is 70 MPa, then breakdown pressure under experimental conditions is given as

$$\text{3D – impermeable scenario } p_w = 0.715\sigma_c + 52.7. \tag{14}$$

$$\text{3D – permeable scenario } p_w = 0.344\sigma_c + 25.4. \tag{15}$$

Eqs. (14) and (15) indicate that the impermeable breakdown pressure is still approximately twice as large as that for the permeable case, which is congruent with experimental observations.

5. Breakdown pressure hypothesis

From the preceding analyses, congruent with two broad sets of experimental data, breakdown pressure is reduced by half where fluid infiltration can occur into the borehole wall. The numerical experiments are employed to demonstrate the effect of fluid infiltration or exclusion into the borehole wall and its corresponding influence on breakdown pressure magnitude. A hypothesis consistent with these observations is that fluid interfacial tension controls whether fluid invades the pore space at the borehole wall and this in turn changes the local stress regime, hence breakdown pressure. Interfacial tension is modulated by fluid state, as sub- or super-critical, and thus gas type and state would be expected to influence the breakdown pressure.

A mixture of supercritical fluids is by definition miscible and will not be excluded from the pore space in the borehole wall by capillarity. Correspondingly, the breakdown pressure for a supercritical fluid should correspond to the permeable solution, whereas the response of a subcritical fluid should correspond to that of the impermeable solution. Eqs. (14) and (15) are the breakdown solutions for the experimental geometry in Fig. 8 that is only approximated by infinite length boreholes and the analytical solutions of Eqs. (5) and (9). In order to apply Eqs. (14) and (15) to explore this hypothesis, the first

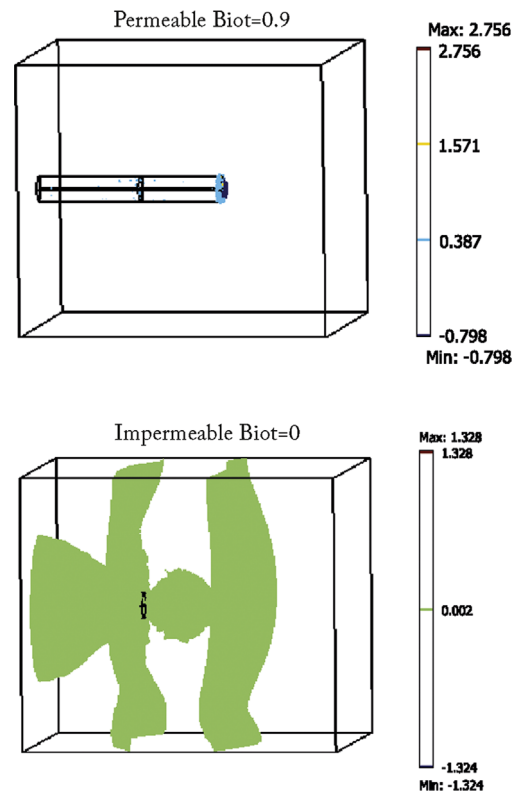


Fig. 11. Spatial distribution of longitudinal stress over fluid pressure for Biot coefficient equal to 0.9 (top) and 0 (down).

important step is to identify the state of the injected fluids. The distribution of fluid states at failure is defined by the experimental fracture breakdown pressures and corresponding transition pressures to supercriticality, as shown in Fig. 3. For the particular experimental conditions: nitrogen, helium and argon are all supercritical, while carbon dioxide, sulfur hexafluoride, and water are subcritical.

The concept of invasion pressure is invoked to represent the response in the borehole wall. If the fluid pressure in the borehole exceeds the critical invasion pressure P_c then the fluids will penetrate the borehole wall and the hoop stress around the wellbore will be correspondingly elevated. We define the critical invasion pressure as the minimum pressure required to force subcritical fluid into the pore space through the pore throat. This may be defined based on scaling arguments as a function of permeability, porosity and interfacial tension as in the Leveret

function (J). This function is defined as

$$J = \frac{P_c}{\sigma} \sqrt{\frac{k}{n}} \quad (16)$$

where σ is the fluid interfacial tension, k is the permeability, P_c is the critical invasion pressure and n is the porosity. For supercritical fluids, interfacial tension is small and invasion of the borehole wall occurs at pressure P_c and results in a lowered breakdown pressure (relative to where the fluid is excluded). Thus, the critical invasion pressure P_c for a supercritical fluid is always smaller than the invasion pressure for the subcritical fluid.

Fig. 12 illustrates the relationship between critical invasion pressure and breakdown pressure for supercritical/subcritical fluids. Impermeable and permeable breakdown pressure solutions give two bounded values. There are three scenarios depending on the critical invasion pressure magnitude:

1. When the invasion pressure is lower than the breakdown pressure for the permeable solution, then both supercritical and subcritical fluids have the same breakdown pressure magnitude (see Fig. 12 left).
2. When the invasion pressure is intermediate between the breakdown pressure for permeable and impermeable solutions, then the subcritical fluid invades and failure occurs at the critical pressure. In this case, supercritical fluids would result in failure at a pressure lower than the invasion pressure (see Fig. 12 center).
3. When the invasion pressure is larger than the breakdown pressure for both permeable and impermeable solutions, then the supercritical fluid causes failure at a lower pressure than for the subcritical fluid (see Fig. 12 right).

Considering that for invasion in any given material of defined permeability and porosity, the ratio of invasion pressure to interfacial tension should be constant as

$$\zeta = \frac{P_b}{\sigma} = \frac{\text{MPa}}{\text{mN/m}} = \frac{10^6 \text{ N/m}^2}{10^{-3} \text{ N/m}} = \frac{10^9}{\text{m}} \quad (17)$$

Then Fig. 13 shows this ratio of breakdown pressure (rather than invasion pressure) to interfacial tension. This is evaluated from the magnitudes of interfacial tension in Table 3. The value ζ is approximately constant for the subcritical fluids, where breakdown is modulated by this invasion parameter. Not only are these breakdown pressures constant but they are also of the expected magnitude of Eq. (17). For the supercritical fluids, there is no relationship for this parameter P_c/σ , suggesting that this behavior is independent of capillary entry pressures – as suggested by the hypothesis. This indicates that the interfacial tension for the subcritical fluid is large enough to govern the breakdown process, while the low interfacial tension of the supercritical fluid has no effect in controlling the breakdown process. For the case of argon where the fluid properties

are supercritical the relation of Eq. (15) is used to define response against the available experimental data of Table 4. Fig. 14 shows the match of the experimental results for Argon with the analytical data showing excellent agreement with the permeable solution. Table 5 summarizes the equations required to calculate fracture breakdown pressure under the conditions corresponding to impermeable/permeable media and resulting in longitudinal/transverse fractures.

6. Conclusions

Expressions are developed based on Biot effective stress theory to predict breakdown pressure for longitudinal and transverse fracture on finite length boreholes. These relationships are used to explore the physical dependencies of fracture breakdown pressures and show that an approximate factor of two exists in the breakdown stress where fluids either invade or are excluded from the borehole wall. These relationships are extended for finite length boreholes to replicate conditions for fracturing experiments in finite-volume samples. These solutions are then used to explain observations of variable breakdown stresses in experiments where all conditions are maintained constant except the composition and state of the fracturing fluids.

The difference in failure response is matched to the state of the fluid – supercritical versus subcritical. Observations suggest that fluid state controls interfacial properties and thereby governs fluid invasion into the matrix and the following breakdown process. The negligible interfacial tension in supercritical fluids allow easy invasion into the matrix, while the subcritical fluid with larger interfacial tension requires a higher pressure to invade and cause

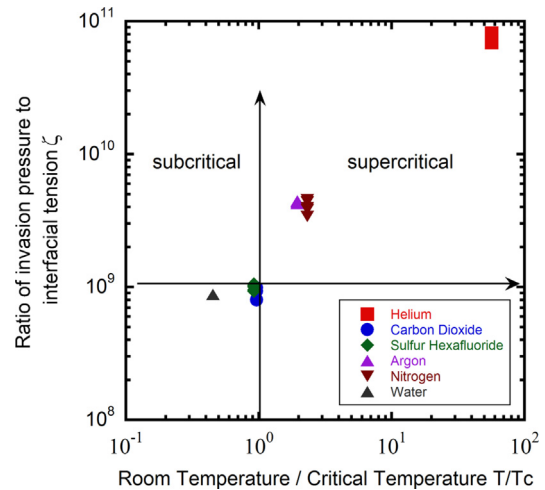


Fig. 13. Distribution of ratio about invasion pressure to the interfacial tension under different fracturing fluids.

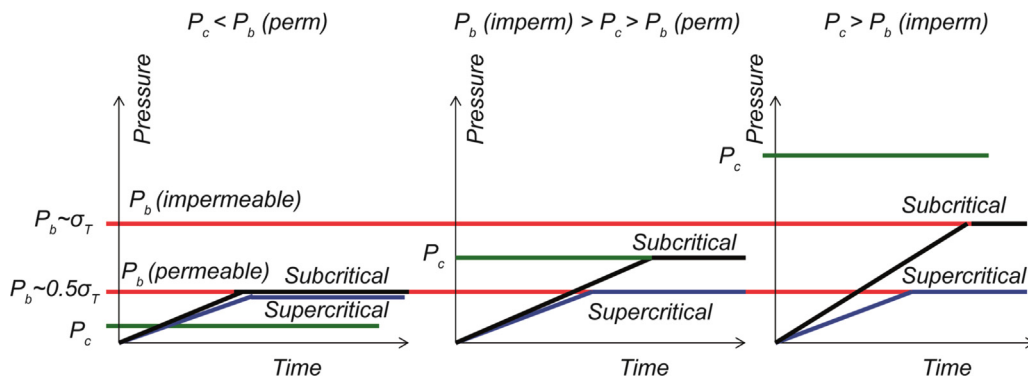


Fig. 12. Summaries of critical pressure vs. breakdown pressure under different invasion pressure P_c values.

Table 3
Comparison of supercritical/subcritical fluid interfacial tension (Berry et al., 1971).

Injected fluid	Interfacial tension (mN/m)
Supercritical fluids	
N ₂	7
He	0.37
Ar	2–13
Non-supercritical fluids	
SF ₆	40–50
CO ₂	72–40
H ₂ O	70–50

Table 4
Breakdown pressure results in hydro-fracture experiment of Argon (Ar) injection under different confining stress from 5 MPa to 60 MPa.

Confining stress (MPa)	Breakdown pressure (MPa)
5	29.85
5	30
5	30.5
30	39.68
40	44.44
50	46.84
60	51.6

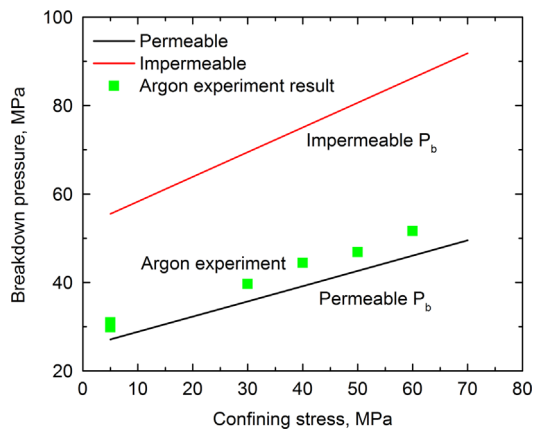


Fig. 14. Validations of 3-D permeable and impermeable breakdown pressure, analytical solutions with experiment data.

Table 5
Summary of expressions for breakdown pressure in different cases: (i) permeable/impermeable medium, (ii) fracture geometry, longitudinal/transverse.

Case no.	Condition	Expression
1	Impermeable medium	$p_w = 0.715\sigma_c + 52.7$
2	Permeable medium	$p_w = 0.344\sigma_c + 25.4$
3	Longitudinal fracture	$p_w = \frac{-3\sigma_{22} + \sigma_{11} + p_0 + \sigma_T}{1 + \eta}$
4	Transverse fracture	$p_w = \frac{-v(3\sigma_{22} - \sigma_{11} + p_0) + \sigma_T}{\eta}$

subsequent breakdown of the borehole. For samples of equivalent permeability and porosity, the ratio of breakdown pressure to interfacial tension is constant for subcritical fluids – identifying the

controlling influence on capillary behavior. Where fluids are supercritical, no similar relationship exists. To the contrary, where the fluid is supercritical, the breakdown pressures are uniformly those predicted where infiltration occurs into the borehole wall – approximately half of the tensile strength of the sample (Fig. 3). These ensemble observations suggest the controlling influence of interfacial tension on breakdown pressure – at least at laboratory scale.

Acknowledgment

This work is the result of support from the Chevron Energy Technology Company. This support is gratefully acknowledged. Originally communicated as paper 13-700 of the 47th US Symposium on Rock Mechanics/Geomechanics, San Francisco. We appreciate the permission of the American Rock Mechanics Association to publish this paper.

References

Alpern, J.S., Marone, C., Elsworth, D., 2012. Exploring the physicochemical process that govern hydraulic fracture through laboratory experiments, Proceedings of the 46th US Rock Mechanics/Geomechanics Symposium. Chicago, IL, USA.

Bennion, B., 2006. The impact of interfacial tension and pore size distribution/capillary pressure character on CO₂ relative permeability at reservoir conditions in CO₂-brine systems, Proceedings of the SPE/DOE Symposium on Improved Oil Recovery. Society of Petroleum Engineer, Tulsa, Oklahoma, USA.

Berry, M.V., Durrans, R.F., Evans, R., 1971. The calculation of surface tension for simple liquids. J. Phys. A: Gen. Phys. 5, 179–180.

Biot, M.A., 1941. General theory of three-dimensional consolidation. J. Appl. Phys. 12 (2), 155–164.

Detournay, E., Cheng, A., 1992. Influence of Pressurization Rate on the Magnitude of Breakdown Pressure, Rock Mechanics. In: Tillerson, J.R., Wawersik, W.R. (Eds.), Rock Mechanics. Balkeman Publishers, Rotterdam, The Netherlands, pp. 325–333.

Escobedo, J., Mansoori, G.A., 1996. Surface tension prediction for pure fluids. AIChE J. 42 (5), 1425–1433.

Gan, Q., Alpern, J.S., Marone, C., Connolly, P., Elsworth, D., 2013. Breakdown pressures due to infiltration and exclusion in finite length boreholes, Proceedings of the 47th U.S. Rock Mechanics/Geomechanics Symposium, June, pp. 13–700.

Garagash, D., Detournay, E., 1996. Influence of pressurization rate on borehole breakdown pressure in impermeable rocks, Proceedings of the 2nd North American Rock Mechanics Symposium. Balkema.

Haimson, B., Fairhurst, C., 1967. Initiation and extension of hydraulic fractures in rocks. Soc. Pet. Eng. 7, <http://dx.doi.org/10.2118/1710-PA>.

Hubbert, M.K., Willis, D.G., 1957. Mechanics of hydraulic fracturing. Trans. Am. Inst. Min. Eng. 210, 53–168.

Kutter, H.K., 1970. Stress analysis of a pressurized circular hole with radial cracks in a infinite elastic plate. Int. J. Fract. 6, 233–247.

Jaeger, J.C., Cook, N.G.W., 1979. Fundamentals of Rock Mechanics, 4th ed. 2009. Wiley, Hoboken, NJ p. 488 pp.

Leake, S.A., Hsieh, P.A., 1997. Simulation of Deformation of Sediments from Decline of Ground-Water Levels in an Aquifer Underlain by a Bedrock Step, edited by U. S. G. S. O. F. Report.

Newman, J.C., 1971. An improved method of collocation for the stress analysis of cracked plates with various shaped boundaries. NASA TN, 1–45.

Solberg, P., Lockner, D., Byerlee, J.D., 1980. hydraulic fracturing in granite under geothermal conditions. Int. J. Rock Mech. Min. Sci. Geomech. Abstr. 17, 25–33.

Timoshenko, S.P., Goodier, J.N., 1951. Theory of Elasticity. McGraw Hill Publishing Co.

Tweed, J., Rooke, D.P., 1973. The distribution of stress near the tip of a radial crack at the edge of a circular hole. Int. J. Eng. Sci. 11, 1185–1195.

Wu, H., Golovin, E., Shulkin, Y., Chudnovsky, A., 2008. Observations of hydraulic fracture initiation and propagation in a brittle polymer, Proceedings of the 42nd US Rock Mechanics Symposium and 2nd U.S.-Canada Rock Mechanics Symposium. American Rock Mechanics Association (ARMA), San Francisco.

Zeng, Zhengwen, Roegiers, J.C., 2002. Experimental Observation of injection rate influence on the hydraulic fracturing behavior of a tight gas sandstone, Proceedings of the SPE/ISRM Rock Mechanics Conference. Society of Petroleum Engineers Inc., Irving, Texas.

Zoback, M.D., Rummel, F., Jung, R., Raleigh, C.B., 1977. Laboratory hydraulic fracturing experiments in intact and pre-fractured rock. Int. J. Rock Mech. Min. Sci. Geomech. Abstr. 14, 49–58.